

In situ observation of a stepwise [2 + 2] photocycloaddition process using fluorescence spectroscopy

Received: 28 June 2023

Accepted: 16 October 2023

Published online: 27 November 2023

Check for updates

Meng-Fan Wang^{1,2}, Yun-Hu Deng¹, Yu-Xuan Hong¹, Jia-Hui Gu¹, Yong-Yong Cao³, Qi Liu¹✉, Pierre Braunstein⁴ & Jian-Ping Lang^{1,2}✉

Using highly sensitive and selective in situ techniques to investigate the dynamics of intermediates formation is key to better understand reaction mechanisms. However, investigating the early stages of solid-state reactions/transformations is still challenging. Here we introduce in situ fluorescence spectroscopy to observe the evolution of intermediates during a two-step [2 + 2] photocycloaddition process in a coordination polymer platform. The structural changes and kinetics of each step under ultraviolet light irradiation versus time are accompanied by the gradual increase-decrease of intensity and blue-shift of the fluorescence spectra from the crystals. Monitoring the fluorescence behavior using a laser scanning confocal microscope can directly visualize the inhomogeneity of the photocycloaddition reaction in a single crystal. Theoretical calculations allow us to rationalize the fluorescence behavior of these compounds. We provide a convenient strategy for visualizing the solid-state photocycloaddition dynamics using fluorescence spectroscopy and open an avenue for kinetic studies of a variety of fast reactions.

The real-time monitoring of chemical processes using in situ techniques is key to understanding the nature of the intermediates and reaction mechanisms on time scales ranging from years to picoseconds and space scales from meters to angstroms, and it has attracted considerable attention owing to its impact in catalysis, synthesis, energy transformation, sensing, etc.^{1–5}. However, the sparsity of direct in situ investigation techniques applied to the initial stages of a reaction/transformation, especially in the solid state, constitute a significant challenge^{6,7}.

Solid-state [2+2] photocycloaddition reactions of olefins offer a powerful access to cyclic organic molecules with specific configurations that would be difficult to obtain using solution reaction methods^{8–15}. Although solid-state [2+2] photocycloaddition reactions are well developed, the limited availability of appropriate analytical techniques, the influence of mixtures of unreacted precursors and

intermediates, etc. make it difficult to in situ monitor the progress of solid-state reactions^{16,17}. In particular, when the concentrations of cyclobutane products are very low and ultraviolet (UV) light irradiation maintains for a short time, their accurate monitoring and identification become much more challenge. Consequently, relatively few reports have appeared on the in situ monitoring of specific properties in the course of a photocycloaddition process¹⁸. However, in situ observation of reactions during the entire transformation is particularly important for understanding the dynamic transitions occurring during photocycloaddition reactions¹⁹.

Analytical techniques applicable to photoreactions include nuclear magnetic resonance spectroscopy (NMR)^{20–22}, infrared spectroscopy (IR)¹³, Raman spectroscopy²³, thermal analysis²⁴, and X-ray diffraction (XRD)^{19,25}. However, only a few of these are suitable in our context. In situ NMR is commonly used to monitor the real-time

¹College of Chemistry, Chemical Engineering and Materials Science, Soochow University, Suzhou 215123 Jiangsu, People's Republic of China. ²State Key Laboratory of Organometallic Chemistry, Shanghai Institute of Organic Chemistry, Chinese Academy of Sciences, Shanghai 200032, People's Republic of China. ³College of Biological, Chemical Science and Engineering, Jiaying University, Jiaying 314001 Zhejiang, People's Republic of China. ⁴Institut de Chimie (UMR 7177 CNRS), Université de Strasbourg, 4 rue Blaise Pascal - CS 90032, 67081 Strasbourg, France. ✉e-mail: qi.liu@suda.edu.cn; jplang@suda.edu.cn

generation of reaction products in solution but is not easily employed for the identification of solid-state reaction products. IR and Raman spectroscopy are mainly used to characterize the changes in functional groups during the reaction process, but the interconversion of isomers is difficult to identify. Thermal analysis mainly depends on differences in the weight loss of unreacted precursors and different photo-addition products. However, it takes almost 1 h to collect one data point. In addition, excessive heating often triggers the reverse (thermal) reaction of dissociation²⁴. The XRD technique includes single-crystal X-ray diffraction (SCXRD) and powder X-ray diffraction (PXRD) and although a number of studies are concerned with single-crystal-to-single-crystal (SCSC) transformations in solid-state [2 + 2] photocycloaddition reactions, current reports mainly focus on the initial and final stages of the reaction^{26,27}, lacking in situ observations. Moreover, when the proportions of cyclobutane products generated by short-time illumination are small, the low spatial and time resolution of the XRD technique makes it impossible to detect the local sites or components²⁸. Therefore, more readily accessible in situ methods with high sensitivity and short response times are urgently needed if one aims at understanding the reaction process of photocycloaddition.

Owing to their extremely high sensitivity and good selectivity, fluorescence sensing attracts much attention^{29–32}. Generally, pyridyl olefin ligands involved in photochemical [2 + 2] cycloaddition reactions within coordination polymers (CPs) are conjugated and exhibit strong fluorescence^{13,33}. Their conjugations and structures are modified in the course of the reaction, which affects their luminescence properties^{34,35}. Although a number of studies are concerned with photo-controlled fluorescence in [2 + 2] photocycloaddition reactions, these reports mainly focus on the fluorescence changes at the initial and final stages^{35–37}, lacking in situ observation of the photoreaction process. Therefore, monitoring the whole solid-state [2 + 2] photocycloaddition reaction using in situ fluorescence spectroscopy may

provide deeper insight into structural or composition modifications that occur during the process.

In this work, we introduce, for the first time, a new approach for the in situ observation of the [2 + 2] photocycloaddition process in a one-dimensional (1D) diene-ligand-based CP using fluorescence spectroscopy, and the study of its reaction kinetics (Fig. 1a). This is realized by using our recently reported CP single crystal platform, $[\text{Cd}_2(\text{F-1,3-bpeb})_2(3,5\text{-DBB})_4]$ (**CP1**, F-1,3-bpeb = 4,4'-(5-fluoro-1,3-phenylene)bis(ethene-2,1-diyl)dipyridine; 3,5-HDBB = 3,5-dibromobenzoic acid), which exhibits a controllable two-step [2 + 2] photocycloaddition triggered by the combined effect of temperature and irradiation³⁸. This CP is transformed into the corresponding dicyclobutane product **CP1-2 β** ($[\text{Cd}_4(\mathbf{2}\beta)_2(3,5\text{-DBB})_8]$, $\mathbf{2}\beta$ = syn-3,4,12,13-tetrakis(4-pyridyl)-8,17-bis-fluoro-1,2,9,10-diethano[2.2]metacyclophane) under UV irradiation at 365 nm at 25 °C, while the monocyclobutane compound **CP1-1** ($[\text{Cd}_2(\mathbf{1})(3,5\text{-DBB})_4]$, $\mathbf{1}$ = 4,4'-(3,4-bis(3-fluoro-5-(2-(pyridin-4-yl)vinyl)phenyl)cyclobutane-1,2-diyl)dipyridine) is formed at 365 nm and -50 °C, a temperature which prevents the occurrence of the second step of the [2 + 2] photocycloaddition reaction (Fig. 1b). Because the π -conjugated system is modified during the [2 + 2] photocycloaddition process, all three CPs display fluorescence with different intensities and quantum yields (QYs). Thus, **CP1-1** with a higher intramolecular through-space conjugation (TSC)^{39,40} displays the largest intensity fluorescence and QY compared to the other two compounds. The fluorescence spectra are collected for both steps of the [2 + 2] photocycloaddition of **CP1**, and the corresponding kinetics are examined. Thanks to the high sensitivity of fluorescence spectroscopy, even when the yield of the cyclobutane product is very low and **CP1** is irradiated with UV light for a short period of time, the fluorescence emission intensity still changes significantly; but this cannot be observed by NMR or XRD techniques. Furthermore, laser scanning confocal microscopy (LSCM)⁴¹ is used to directly visualize the [2 + 2] photocycloaddition in a single crystal, which confirms the non-uniform

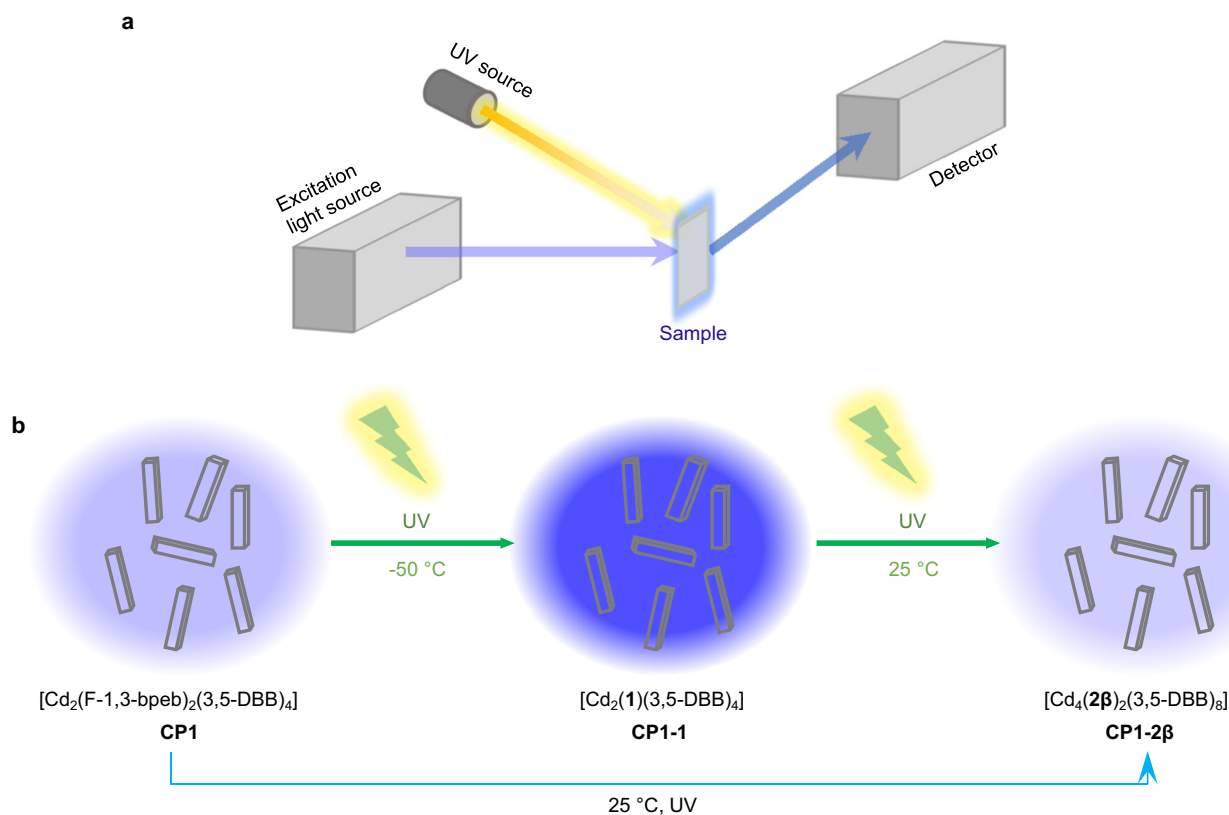


Fig. 1 | Schematic illustration. **a** Schematic diagram of in situ fluorescence spectroscopy. **b** The schematic synthesis routes of the two-step solid-state [2 + 2] photocycloaddition reaction.

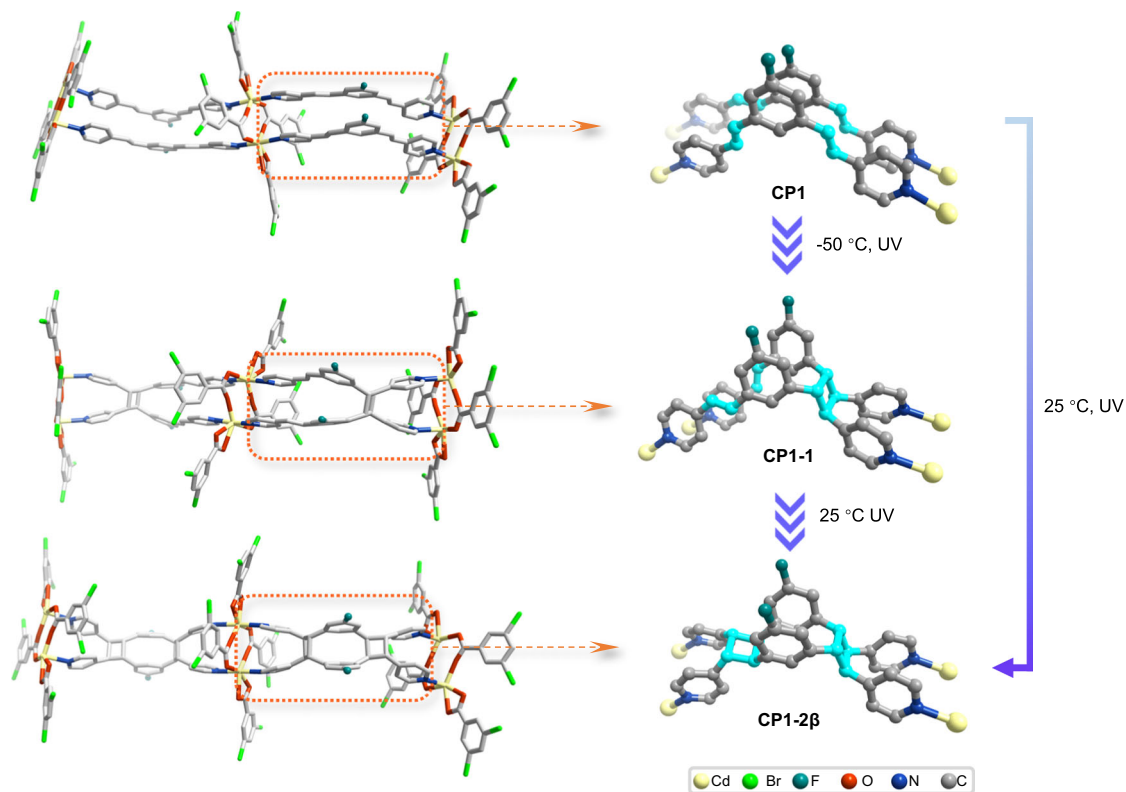


Fig. 2 | Structures of the two-step [2 + 2] photocycloaddition transformation of CP1 to CP1-2β. The 1D chain motifs and structures of **CP1**, **CP1-1** and **CP1-2β** illustrate the monomer transformations for each step. For clarity, hydrogen atoms

have been omitted. The configurations and transformations of C=C groups associated with the above reactions are highlighted in sky blue.

character of the reaction process between the top and bottom parts of the crystal.

Results

Crystal structures and one two-step [2 + 2] photocycloaddition reaction

Colorless crystals of **CP1** were acquired from solvothermal reactions of $3\text{CdSO}_4 \cdot 8\text{H}_2\text{O}$ with F-1,3-bpeb and 3,5-HDBB according to the previous work³⁸. SCXRD analysis revealed that **CP1** crystallizes in the *Pi* space group and the asymmetric unit contains a $[\text{Cd}_2(\text{F-1.3-bpeb})_2(3,5\text{-HDBB})_2]$ unit. **CP1** was previously shown to contain the diene ligands, F-1,3-bpeb, linked by Cd^{2+} ions and second carboxylate ligand 3,5-HDBB to give a one-dimensional (1D) zigzag chain structure. Two pairs of C=C bonds in each set of the adjacent F-1,3-bpeb ligands hold different conformations in the chain of **CP1**. One pair of C=C bonds is aligned to be parallel with a separation of 3.82 Å while the other pair is arranged in a crisscross fashion with a distance of 3.69 Å (Fig. 2 and Supplementary Fig. 1). According to Schmidt's criteria⁴², only the pair of parallel C=C bonds in two opposite F-1,3-bpeb ligands can undergo a photocycloaddition reaction.

Our prediction from the C=C arrangement in **CP1** (Fig. 2) is that **CP1-1** would be the photodimerization product from **CP1**. However, **CP1-2β** was obtained after **CP1** got irradiated under UV light (2 W LED lamp, $\lambda = 365$ nm) for 1 h at 25 °C while **CP1-1** was generated after **CP1** was irradiated under UV light in 10 min at -50 °C and converted to **CP1-2β** in a further 35 min irradiation at 25 °C in an SCSC fashion, indicating that the C=C groups in the crisscross manner rotates to the parallel position under UV light and 25 °C^{43,44}. When **CP1** was exposed to UV light at -50 °C, which greatly blocked the molecular rotation, only the parallel C=C groups experienced dimerization while those arranged in a crisscross manner remained intact, leading to the formation of **CP1-1**. Time-dependent ^{19}F NMR spectra showed that the monocyclobutane

product was first formed and gradually converted to the dicyclobutane species when **CP1** got irradiated under UV light at 25 °C (Supplementary Fig. 2). SCXRD results, supported by ^{19}F NMR data, indicated that **CP1-1** can be viewed as an intermediate during the formation of **CP1-2β** from **CP1** (Fig. 2 and Supplementary Figs. 3, 4). The conversion of vinyl ligands to cyclobutane affected photophysical properties of these CPs, which is revealed by the UV-vis adsorption spectra of **CP1** irradiated under UV light at room temperature (Supplementary Fig. 5). Its absorption edge gradually blue-shifted to 390 nm due to the breaking of the π -conjugation of the cyclobutane ligands⁴⁵⁻⁴⁷.

In situ fluorescence study

Compounds **CP1**, **CP1-1** and **CP1-2β** are stable in air and retain their crystalline structures intact even when immersed in ethanol for 24 h (Supplementary Fig. 6). These three compounds emitted blue light (λ_{em} 451 nm for **CP1**; λ_{em} 437 nm for **CP1-1**; λ_{em} 437 nm for **CP1-2β**) in the solid state, with QYs of 7.8%, 58.5%, and 1.2% under excitation at 365 nm at room temperature, respectively (Supplementary Fig. 7 and Supplementary Table 1). It showed approximately the same excitation and emission wavelengths as ligand F-1,3-bpeb, suggesting that the emission from **CP1**, **CP1-1**, and **CP1-2β** is of the ligand-to-ligand and intra-ligand charge transfer type (Supplementary Fig. 7).

Collecting the in situ fluorescence spectra of samples of **CP1** continuously irradiated to **CP1-2β** at 25 °C revealed strong variations during the photocycloaddition reaction, the emission intensity increasing by 45 times after irradiation under UV light for 3 min and blue-shifted to 437 nm, followed by a gradual decrease, although it contained both steps of the [2 + 2] photocycloadditions throughout (Fig. 3a, d). It is worth noting that powder samples of **CP1** showed a drastic fluorescence enhancement of 2.7 times after UV light irradiation for only 1 s, while the ^{19}F NMR data collected after 10 s were still the same as the original ones, indicating the high sensitivity of

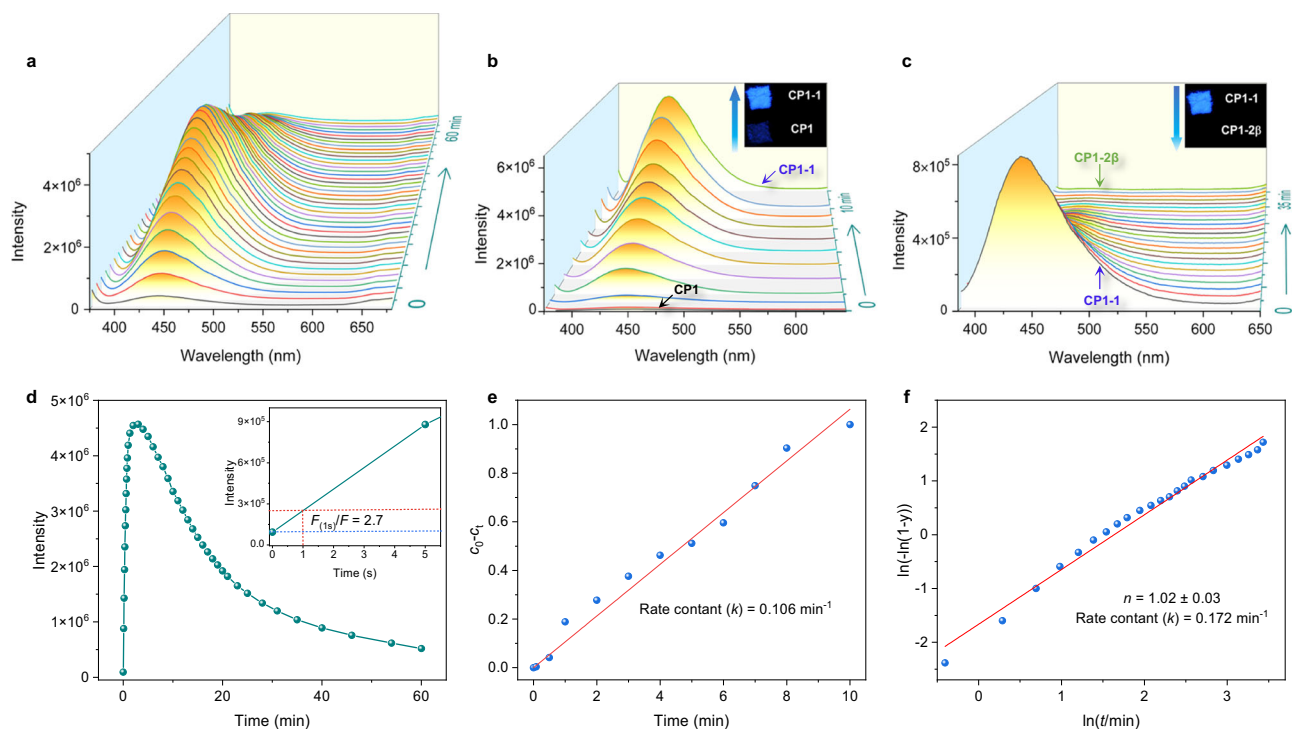


Fig. 3 | In situ fluorescence spectra. **a** The in situ time-dependent fluorescence spectra of **CP1** irradiated with UV light at 25 °C ($\lambda_{\text{ex}} = 365$ nm). **b** The in situ time-dependent fluorescence spectra of **CP1** irradiated with UV light at -50 °C ($\lambda_{\text{ex}} = 365$ nm). Inset: the photographs of **CP1** and **CP1-1** under UV light irradiation. **c** The in situ time-dependent fluorescence spectra of **CP1-1** irradiated with UV light at 25 °C ($\lambda_{\text{ex}} = 365$ nm). Inset: the photographs of **CP1-1** and **CP1-2 β** under UV light irradiation. **d** Plots of relative fluorescence emission intensity at 437 nm of **CP1** irradiated under 365 nm at 25 °C ($\lambda_{\text{ex}} = 365$ nm). Inset: Enlargement of the fluorescence emission intensity at 437 nm of **CP1** irradiated at 365 nm and 25 °C. F and $F_{(15)}$

represent the original fluorescence emission intensity at 437 nm of **CP1** and that after 1 s of 365 nm UV irradiation at 25 °C, respectively. **e** Plots of $c_0 - c_t$ versus time in the transformation from **CP1** to **CP1-1**. c_0 and c_t represent the conversion (mole fraction) calculated from fluorescence intensity data sets of **CP1** before and at any irradiation time (t) at 365 nm and -50 °C, respectively. k is the rate constant. **f** Plots of $\ln(-\ln(1-y))$ versus $\ln(\text{time})$ fitted by JMAK model in the transformation from **CP1-1** to **CP1-2 β** . y is the conversion (mole fraction) of the photoproduct calculated from fluorescence intensity data sets of **CP1-1** irradiated at 365 nm and 25 °C. k is the rate constant, and n is the dimensionality of growth (Avrami exponent).

fluorescence spectroscopy which allowed changes to be monitored even when the yield of the cyclobutane product was very low in a short time of UV irradiation. The advantage of fluorescence spectroscopy may come from its absolute counting way, which provided intensity as high as order of magnitude of 10^6 (Fig. 3). Furthermore, a series of fluorescence photographs of this process were recorded as a function of irradiation time. As shown in Supplementary Fig. 8, increases and decreases of fluorescence of the powder of **CP1** were clearly observed, which is consistent with the fluorescence spectral data. Such a phenomenon encouraged us to study systematically the photocycloaddition reaction by in situ fluorescence spectroscopy.

During the [2 + 2] photocycloaddition from **CP1** to **CP1-1** at -50 °C under UV light, the emission intensity increased gradually and blue-shifted to 437 nm in 10 min (Fig. 3b). The emission intensity of **CP1-1** was about 71 times higher than that of **CP1**, and its absolute QY was 58.5%. Subsequently, on going from **CP1-1** to **CP1-2 β** , the emission intensity decreased following the UV light irradiation, resulting in about 1/20 of the intensity of **CP1-2 β** compared to **CP1-1**, with an absolute QY of 1.2% (Fig. 3c). The fluorescence lifetime (τ) of **CP1**, **CP1-1** and **CP1-2 β** were 6.8 ns, 13.9 ns and 5.4 ns, respectively, confirming the fluorescence feature for all of them (Supplementary Fig. 9).

We researched the kinetics of each step from the results of the in situ time-dependent fluorescence data. The fitting of the conversion data calculated from fluorescence intensity versus irradiation time showed different kinetics for **CP1** to **CP1-1** and **CP1-1** to **CP1-2 β** , respectively (Fig. 3e, f). During the transformation from **CP1** to **CP1-1**, a fitting of the conversion percentage of **CP1-1** versus UV light irradiation time at -50 °C resulted in a linear relationship of $c_0 - c_t$ with the irradiation time, indicating a zero-order behavior^{48,49} for the first step from

CP1 to **CP1-1** with a rate constant of 0.106 min^{-1} , where c_0 and c_t represent the conversion (mole fraction) calculated from fluorescence intensity data sets of **CP1** before and at any irradiation time (t) at 365 nm and -50 °C, respectively (Fig. 3e). The kinetics of the transformation from **CP1-1** to **CP1-2 β** was fitted by applying the Johnson-Mehl-Avrami-Kolmogorov (JMAK) model, which has been successfully applied previously to a number of [2 + 2] photocycloadditions^{16,24,50}. The JMAK kinetics are described by Eq. (1):

$$y = 1 - e^{-(kt)^n} \quad (1)$$

where y is the conversion (mole fraction) of the photoproduct formed in time t , k is the rate constant, and n is the dimensionality of growth (Avrami exponent). The plot of $\ln(-\ln(1-y))$ versus $\ln(\text{time})$ was fitted to attain an Avrami exponent of (1.02 ± 0.03) , indicating a first-order behavior for the second step from **CP1-1** to **CP1-2 β** with a rate constant of 0.172 min^{-1} (Fig. 3f). The exponential trends in the mole ratio determined by ^{19}F NMR closely resemble the trends determined by in situ fluorescence intensity (Supplementary Figs. 10–12). In addition, a linear relationship between the conversion calculated from ^{19}F NMR and the fluorescence data for both steps could be fitted, indicating that the conversions obtained from in situ fluorescence intensity can be used similarly to those determined by ^{19}F NMR (Supplementary Fig. 13). The deviation of linearity might be due to the inhomogeneity of [2 + 2] photocycloaddition reaction that originated from non-uniform irradiation geometry, which was observed in the LSCM data.

In order to directly visualize the fluorescence changes within a single crystal during the [2 + 2] photocycloaddition reaction process, LSCM of **CP1** irradiated under UV light was collected at room

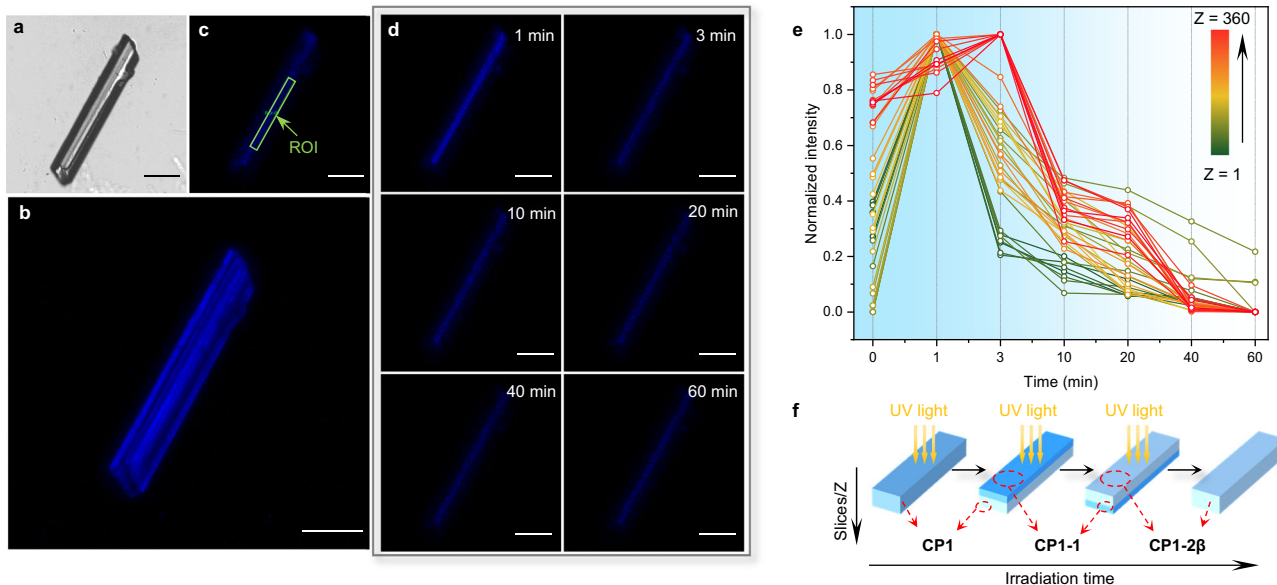


Fig. 4 | Three-dimensional (3D) LSCM tomograph of CPI. **a** Bright-field image and **b** 3D reconstruction of CPI, scale bars are 50 μm . **c** LSCM images of CPI and **d** CPI irradiated at 25 $^{\circ}\text{C}$ with UV light for some time intervals, at the top first slice, scale bars are 50 μm . **e** Quantified luminescence intensities in (c) ROI (regions of interest)

range for CPI after different irradiation times at different slices. Z represents the different slices in a single crystal. **f** Schematic illustration of the change of fluorescence intensity in a single crystal of CPI under UV light irradiation at 25 $^{\circ}\text{C}$.

temperature and analyzed. The high resolution of LSCM enabled us to observe the details of fluorescence change at each layer of the crystal upon UV light irradiation. Firstly, we examined the reliability of this technique by collecting data for CPI without UV light irradiation for 1 h, with every step of 5 s. The blue fluorescence was clearly observed and its intensity was constant (Supplementary Fig. 14).

Then layer scanning from this CPI single crystal at different UV light irradiation times ($t = 0, 1, 3, 10, 20, 40, 60$ min) at 25 $^{\circ}\text{C}$ was performed from the plane perpendicular to the top of the crystal, with a thickness of 100 nm for each slice (Fig. 4a–d and Supplementary Fig. 15). As shown in Fig. 4d, e and Supplementary Fig. 16, the fluorescence intensity in the same layer first gradually increased and then decreased with irradiation time, consistent with the transformations of CPI generating CPI-1 and CPI-2 β sequentially, as shown from fluorescence spectra results (Fig. 3). However, the fluorescence intensity was found to change at different depths of the crystal. To gain further insight into the fluorescence intensity changes at different depths of the crystal, we quantified the fluorescence intensities at different depths as a function of exposure time (t) by employing the z-stacked scan of LSCM which recorded a series of fluorescence snapshot images (Fig. 4e and Supplementary Fig. 16). As evident in Fig. 4e and f, from the 1st to the 260th slices, i.e., for the top part of the crystal, the fluorescence intensity reached a maximum after 1 min of irradiation, while after the 260th slice (ca. 26 μm deep in the crystal), the highest fluorescence intensity was reached after 3 min of illumination, showing that the photocycloaddition reaction occurred slower in the lower layer than in the top part of the crystal. The photocycloaddition reaction in the single crystal of CPI first generated CPI-1 on the top layers under UV light irradiation at 25 $^{\circ}\text{C}$, accompanied by increase of fluorescence intensity in this part. As the irradiation went on, the lower part of the crystal began to gradually form CPI-1, and the top part was converted from CPI-1 to CPI-2 β , accompanied by a brightening in fluorescence of the lower part and a darkening of the top part (Fig. 4f). Monitoring of the [2+2] photocycloaddition reaction by following the changes in fluorescence intensity clearly indicated that the [2+2] photocycloaddition reaction started from the top of the crystal (UV-exposed side) and gradually reached the bottom layers.

Mechanism study

The solid-state electron spin resonance (ESR) spectra of CPI were measured at room temperature to exclude interference from radical species that have been reported to be responsible for some extrinsic emissions⁵¹. An electron paramagnetic resonance (EPR) signal was found in CPI, and the signal at $g = 2.0024$ is consistent with stable organic radicals (Supplementary Fig. 17). After irradiation under UV light ($\lambda \leq 360$ nm) for 2 min and 5 min, no obvious changes were noticed, indicating that radical species were not involved in the fluorescence change of the [2+2] photocycloaddition process⁵².

Hirshfeld surface analyses of the structures of the repetitive units, $[\text{Cd}_4(\text{F-1.3-bpeb})_2(3,5\text{-DBB})_4]$ in CPI, $[\text{Cd}_4(\mathbf{1})(3,5\text{-DBB})_4]$ in CPI-1 and $[\text{Cd}_4(\mathbf{2}\beta)(3,5\text{-DBB})_4]$ in CPI-2 β , were conducted and showed similar proportions of intermolecular interactions (Supplementary Figs. 18 and 19). To understand the detailed mechanism of the different QYs associated with CPI, CPI-1 and CPI-2 β , simplified time-dependent density functional theory (sTDDFT) calculations were utilized to simulate the ground- and excited-state frontier molecular orbitals^{39,52}. The molecular orbital surfaces of the highest occupied molecular orbital (HOMO) and lowest unoccupied molecular orbital (LUMO) clearly show that the fluorescence emission band of compound CPI, CPI-1 and CPI-2 β originates from ligand-to-ligand and intra-ligand charge transfer (Fig. 5). First for CPI, in both the ground-state and the excited state, LUMO is mainly on the F-1,3-bpeb ligand, in which there is a large π -conjugation. This means that the fluorescence emission from CPI is attributed to the intrinsic through-bond conjugation (TBC)⁵³ from the F-1,3-bpeb ligands. When CPI-1 is formed, one pair of C=C bonds reacted to form cyclobutane, partially destroying the electronic conjugation within the F-1,3-bpeb ligands (Supplementary Fig. 18). However, because of the connection between two F-1,3-bpeb ligands, intramolecular TSC was observed between them, with an obvious electronic overlap involving the two adjacent pyridine vinyl groups (LUMO of CPI-1) (Fig. 5 and Supplementary Fig. 20). In contrast, two cyclobutanes are formed in CPI-2 β , which is a non-conjugated organic compound. The nature of the LUMO of CPI-2 β showed that there is an electronic overlapping between the two adjacent pyridine rings, thereby forming intramolecular TSC in it (Fig. 5 and Supplementary Fig. 20). The larger HOMO-LUMO gaps of CPI-1

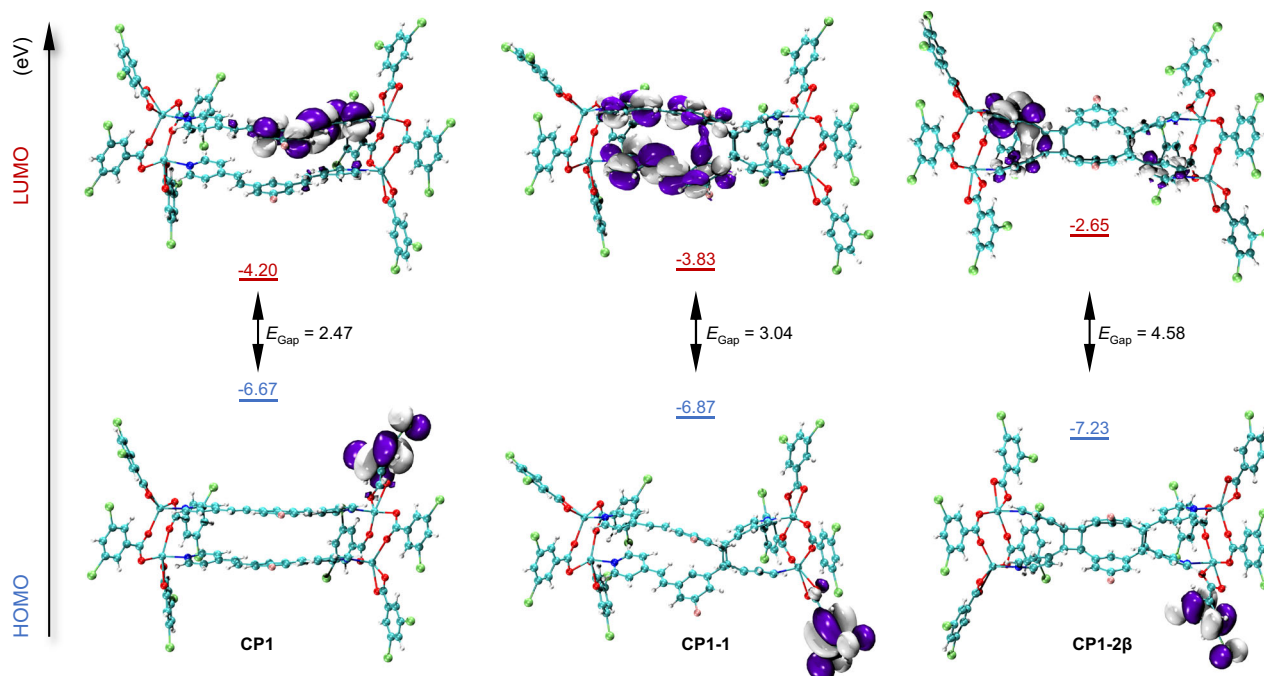


Fig. 5 | Theoretical calculations of CP1, CP1-1, and CP1-2 β . Frontier molecular orbitals of optimized excited-state geometries of **CP1**, **CP1-1**, and **CP1-2 β** calculated

by the sTDDFT method at the PBE0 D3 def2-TZVP level, ORCA 5.0.3 package⁶³. E_{Gap} represents calculated energy gap.

and **CP1-2 β** compared to **CP1** is also consistent with the blue-shift of the fluorescence spectra on going from **CP1-1** and **CP1-2 β** to **CP1**. A combination of intramolecular TSC and TBC in **CP1-1** relative to TBC in **CP1** and intramolecular TSC in **CP1-2 β** can account for their different fluorescence properties. In addition, the dimensionless oscillator strength (f_{osc}) of **CP1-1** and **CP1-2 β** in the crystal state was calculated. The f_{osc} of **CP1-1** and **CP1-2 β** from the S_0 to S_1 states are 0.000054 and 0.000005, respectively. The larger oscillator strength could help to elucidate the bright fluorescent emission in **CP1-1**, as revealed from fluorescence spectra results and LSCM images (Figs. 3 and 4)⁵⁴.

In summary, in situ fluorescence spectroscopy was introduced to monitor the controllable two-step [2 + 2] photocycloaddition process in a CP platform, where the structural changes under UV light irradiation versus time were accompanied by the gradual increase-decrease of intensity and blue-shift of the fluorescence spectra of the CP crystals. This technique showed much higher sensitivity compared to other ones and the related kinetics of each step were investigated, revealing different behaviors for each step, as also confirmed by NMR spectroscopy. In addition, LSCM of a single crystal was performed to directly visualize the change of fluorescence during the [2 + 2] photocycloaddition process. A horizontally uniform and vertically uneven transformation of the crystal was established, depending on the UV light irradiation orientation. Finally, combined theoretical calculations and crystal structure analyses indicated that intramolecular TSC plays an important role in the different fluorescence behaviors of these compounds. This work not only provides a practical strategy for the visualization of [2 + 2] photocycloaddition process but may also open new perspectives for the kinetic study of diverse fast inorganic and/or organic reactions.

Methods

Sample preparation for fluorescence measurement

The sample is sandwiched between two quartz pieces for testing. For **CP1** as an example: the original crystals were placed into a mortar and ground into a powder. Next, 3 mg of the powder was dispersed evenly in ethanol (3 mL), and the suspension (100 μL) was dropped on one quartz piece (12 \times 20 mm), dried in the air, and then covered with the

other piece of quartz to prepare the sample. The sample thickness was about 0.1 mm.

Photo-irradiation experiments

The original crystals of **CP1** or **CP1-1** were placed into a mortar and ground into powder. Next, the powder (3 mg) was dispersed evenly in ethanol (3 mL), and the suspension (200 μL) was dropped on one quartz piece (25 \times 25 mm), dried in the air to prepare the sample. The sample thickness was about 0.1 mm.

Sample irradiated at room temperature: the sample on the quartz pieces was irradiated with a LED lamp (365 nm, 2 W) for a period of time to form the photoproduct. The distance between the sample and the UV source was fixed to be ca. 10 cm.

Sample irradiated at -50°C : **CP1** deposited on the quartz pieces was placed in a long glass tube which was immersed in a low-temperature thermostatic reaction bath at -50°C and irradiated with a LED lamp (365 nm, 2 W) for a period of time to form the photoproduct. The distance between the sample and the UV source was fixed at ca. 17 cm.

LSCM studies

The block crystals of **CP1** were suspended in ethanol and placed between a pair of glasses. The **CP1** crystals were excited at 405 nm with a semiconductor laser, and the emission was collected at 515–600 nm in the blue channel. The QYs of **CP1**, **CP1-1**, and **CP1-2 β** excited at 405 nm show the same trend as those at 365 nm ($\text{QY}_{\text{CP1-1}} > \text{QY}_{\text{CP1}} > \text{QY}_{\text{CP1-2}\beta}$, Supplementary Table 1). The results of two **CP1** single crystals with different sizes were displayed. One was selected for testing focal depth and 3D reconstruction, and the other one was used for time-series scan. The first **CP1** single crystal examined had an irregular hexahedral shape with a size of around 233.4 \times 38.1 μm . The z-stack scan was examined from the plane perpendicular to the top of the crystal by 427 slices, with a thickness of 100 nm for each slice, from which a 3D reconstruction of the crystal was generated. All of the images were obtained using the same settings. The external UV light source (365 nm, 2 W) was irradiated from a plane perpendicular to the top of the crystal, and the distance between the crystal and the light

source was ca. 10 cm. The time-series scan of **CPI** single crystal was collected every 5 s until 1 h.

Computational methods

The theoretical calculations on **CPI**, **CPI-1** and **CPI-2 β** were performed for molecules in vacuum. On the basis of the crystal structures, the repetitive units, $[\text{Cd}_4(\text{F-1.3-bpeb})_2(3,5\text{-DBB})_4]$ in **CPI**, $[\text{Cd}_4(\mathbf{1})(3,5\text{-DBB})_4]$ in **CPI-1** and $[\text{Cd}_4(\mathbf{2\beta})(3,5\text{-DBB})_4]$ in **CPI-2 β** , were selected as the initial calculation model. The lowest energy conformations of all compounds at the ground state and the excited state were optimized by B3LYP functional with mixed basis set, 6-311G(d) for C, H, O, N, F, Br, and Lanl2dz for Cd. The XYZ coordinates of optimized geometries are provided as source data in the source file. Gaussian 09 program was used for density functional theory (DFT) calculations⁵⁵. Single-point energy and excited state calculations were implemented by PBE0 hybrid functional with def2-TZVP basis set, def2-J auxiliary basis set, and RI-approximation using ORCA quantum chemistry software (Version 5.0.3)^{54,56,57}. Grimme's D3BJ dispersion correction was applied to further describe long-range inter/intramolecular interactions⁵⁸. The relativistic effective core potential (ECP) for Cd was used in all calculations⁵⁹. Vertical excitation energy and orbital distribution of the excited states were calculated through the simplified time-dependent density functional theory (sTDDFT) method at optimized ground state geometry. The distribution of frontier molecular orbitals and electronic transition of singlet states were analyzed on Multiwfn 3.8 software⁶⁰. The Visual Molecular Dynamics (VMD) program was utilized to obtain the color-filled isosurfaces orbitals graphs⁶¹. The Hirshfeld surfaces and decomposed fingerprint plots were calculated and mapped using CrystalExplorer 21.5 package⁶².

Data availability

Synthetic and experimental procedures, as well as fluorescence spectra, NMR spectra, PXRD, and computational data, are provided in the Supplementary Information. Crystallographic data for the structures reported in this article have been deposited at the Cambridge Crystallographic Data Centre, under deposition numbers CCDC 1889155 (**CPI**), 2036562 (**CPI-1**), and 2036563 (**CPI-2 β**). Copies of the data can be obtained free of charge via <https://www.ccdc.cam.ac.uk/structures/>. Data are also available from the corresponding author upon request. Source data are provided with this paper.

References

- Zhao, E. W. et al. In situ NMR metrology reveals reaction mechanisms in redox flow batteries. *Nature* **579**, 224–228 (2020).
- Wang, C. et al. Different timescales during ultrafast stilbene isomerization in the gas and liquid phases revealed using time-resolved photoelectron spectroscopy. *Nat. Chem.* **14**, 1126–1132 (2022).
- Morris, S. A. et al. In situ solid-state NMR and XRD studies of the ADOR process and the unusual structure of zeolite IPC-6. *Nat. Chem.* **9**, 1012–1018 (2017).
- Hess, C. New advances in using Raman spectroscopy for the characterization of catalysts and catalytic reactions. *Chem. Soc. Rev.* **50**, 3519–3564 (2021).
- Lyu, J. et al. Phase transitions in metal-organic frameworks directly monitored through in situ variable temperature liquid-cell transmission electron microscopy and in situ X-ray diffraction. *J. Am. Chem. Soc.* **142**, 4609–4615 (2020).
- Prins, P. T. et al. The formation of $\text{NaYF}_4:\text{Er}^{3+}, \text{Yb}^{3+}$ nanocrystals studied by in situ X-ray scattering: phase transition and size focusing. *Angew. Chem. Int. Ed.* **62**, e202305086 (2023).
- Li, J. J. & Deepak, F. L. In situ kinetic observations on crystal nucleation and growth. *Chem. Rev.* **122**, 16911–16982 (2022).
- Skubi, K. L. & Yoon, T. P. Organic chemistry: shape control in reactions with light. *Nature* **515**, 45–46 (2014).
- Poplata, S., Troster, A., Zou, Y. Q. & Bach, T. Recent advances in the synthesis of cyclobutanes by olefin [2+2] photocycloaddition reactions. *Chem. Rev.* **116**, 9748–9815 (2016).
- Ramamurthy, V. & Sivaguru, J. Supramolecular photochemistry as a potential synthetic tool: photocycloaddition. *Chem. Rev.* **116**, 9914–9993 (2016).
- Lei, T. et al. General and efficient intermolecular [2+2] photodimerization of chalcones and cinnamic acid derivatives in solution through visible-light catalysis. *Angew. Chem. Int. Ed.* **56**, 15407–15410 (2017).
- Campillo-Alvarado, G. et al. Exploiting boron coordination: B \leftarrow N bond supports a [2+2] photodimerization in the solid state and generation of a diboron bis-tweezer for benzene/thiophene separation. *Angew. Chem. Int. Ed.* **58**, 5413–5416 (2019).
- Yu, J. G., Gan, M. M., Bai, S. & Han, Y. F. Photodriven solid-state multiple [2+2] cycloaddition strategies for the construction of polycyclobutane derivatives. *CrystEngComm* **21**, 4673–4683 (2019).
- Wang, M. F. et al. Coordination-driven stereospecific control strategy for pure cycloisomers in solid-state diene photocycloaddition. *J. Am. Chem. Soc.* **142**, 700–704 (2020).
- Yang, S. Y., Naumov, P. & Fukuzumi, S. Topochemical limits for solid-state photoreactivity by fine tuning of the π - π interactions. *J. Am. Chem. Soc.* **131**, 7247–7249 (2009).
- Medishetty, R. et al. Single crystals popping under UV light: a photosensitive effect triggered by a [2+2] cycloaddition reaction. *Angew. Chem. Int. Ed.* **53**, 5907–5911 (2014).
- Hallmann, J. et al. Time-resolved X-ray diffraction of the photochromic α -styrylpyrylium trifluoromethanesulfonate crystal films reveals ultrafast structural switching. *J. Am. Chem. Soc.* **131**, 15018–15025 (2009).
- Hu, F. L., Wang, S. L., Lang, J. P. & Abrahams, B. F. In-situ X-ray diffraction snapshotting: determination of the kinetics of a photodimerization within a single crystal. *Sci. Rep.* **4**, 6815 (2014).
- Claassens, I. E., Barbour, L. J. & Haynes, D. A. A multistimulus responsive porous coordination polymer: temperature-mediated control of solid-state [2+2] cycloaddition. *J. Am. Chem. Soc.* **141**, 11425–11429 (2019).
- Toh, N. L., Nagarathinam, M. & Vittal, J. J. Topochemical photodimerization in the coordination polymer $[(\text{CF}_3\text{CO}_2)(\mu\text{-O}_2\text{CCH}_3)\text{Zn}_2(\mu\text{-bpe})_2]_n$ through single-crystal to single-crystal transformation. *Angew. Chem. Int. Ed.* **44**, 2237–2241 (2005).
- Trimble, J. S. et al. A designed photoenzyme for enantioselective [2+2] cycloadditions. *Nature* **611**, 709–714 (2022).
- Sun, N. et al. Enantioselective [2+2]-cycloadditions with triplet photoenzymes. *Nature* **611**, 715–720 (2022).
- Chen, D. et al. In situ Raman monitoring of [2+2] cycloaddition of pyridine substituted olefins induced by visible laser. *Chem. Commun.* **50**, 15631–15633 (2014).
- Panda, T. & Naumov, P. Time-dependent photodimerization of α -trans-cinnamic acid studied by photocalorimetry and NMR spectroscopy. *Cryst. Growth Des.* **18**, 2744–2749 (2018).
- Rath, B. B. & Vittal, J. J. Photoreactive crystals exhibiting [2+2] photocycloaddition reaction and dynamic effects. *Acc. Chem. Res.* **55**, 1445–1455 (2022).
- Kusaka, S. et al. Dynamic topochemical reaction tuned by guest molecules in the nanospace of a metal-organic framework. *J. Am. Chem. Soc.* **141**, 15742–15746 (2019).
- Marshall, R. J., Griffin, S. L., Wilson, C. & Forgan, R. S. Single-crystal to single-crystal mechanical contraction of metal-organic frameworks through stereoselective postsynthetic bromination. *J. Am. Chem. Soc.* **137**, 9527–9530 (2015).
- Li, X. et al. Progress and perspective for in situ studies of CO_2 reduction. *J. Am. Chem. Soc.* **142**, 9567–9581 (2020).

29. Zhang, Y. M. et al. Luminescent sensors based on metal-organic frameworks. *Coord. Chem. Rev.* **354**, 28–45 (2018).
30. Lustig, W. P. et al. Metal-organic frameworks: functional luminescent and photonic materials for sensing applications. *Chem. Soc. Rev.* **46**, 3242–3285 (2017).
31. Cui, Y. J., Yue, Y. F., Qian, G. D. & Chen, B. L. Luminescent functional metal-organic frameworks. *Chem. Rev.* **112**, 1126–1162 (2012).
32. Li, S. S. et al. Transition metal-based bimetallic MOFs and MOF-derived catalysts for electrochemical oxygen evolution reaction. *Energy Environ. Sci.* **14**, 1897–1927 (2021).
33. Yang, Z. Y. et al. Assembly of a Zn(II) coordination polymer of tetrapyridyl tetraene ligands for selective sensing of CrO_4^{2-} and Fe^{3+} in water via luminescence quenching and enhancement. *CrystEngComm* **24**, 1564–1572 (2022).
34. Mizobe, Y. et al. Systematic investigation of molecular arrangements and solid-state fluorescence properties on salts of anthracene-2,6-disulfonic acid with aliphatic primary amines. *Chem* **15**, 8175–8184 (2009).
35. Li, N. Y. et al. Controllable fluorescence switching of a coordination chain based on the photoinduced single-crystal-to-single-crystal reversible transformation of a syn-[2.2]metacyclophane. *Inorg. Chem.* **57**, 849–856 (2018).
36. Li, N. Y., Chen, J. M., Tang, X. Y., Zhang, G. P. & Liu, D. Reversible single-crystal-to-single-crystal conversion of a photoreactive coordination network for rewritable optical memory storage. *Chem. Commun.* **56**, 1984–1987 (2020).
37. Papaefstathiou, G. S., Zhong, Z., Geng, L. & MacGillivray, L. R. Coordination-driven self-assembly directs a single-crystal-to-single-crystal transformation that exhibits photocontrolled fluorescence. *J. Am. Chem. Soc.* **126**, 9158–9159 (2004).
38. Wang, M. F. et al. Controllable multiple-step configuration transformations in a thermal/photoinduced reaction. *Nat. Commun.* **13**, 2847 (2022).
39. Xiong, Z. P. et al. Controllable secondary through-space interaction and clusteroluminescence. *CCS Chem.* 1–13 (2023).
40. Liu, J. et al. Through-space interaction of tetraphenylethylene: what, where, and how. *J. Am. Chem. Soc.* **144**, 7901–7910 (2022).
41. Wang, Y. et al. Molecular vise approach to create metal-binding sites in MOFs and detection of biomarkers. *Angew. Chem. Int. Ed.* **57**, 7120–7125 (2018).
42. Schmidt, G. M. J. Photodimerization in the solid state. *Pure Appl. Chem.* **27**, 647–678 (1971).
43. Harada, J. & Ogawa, K. Pedal motion in crystals. *Chem. Soc. Rev.* **38**, 2244–2252 (2009).
44. Xiao, C. Y., Xi-Ling Deng, X. L., Wei, Z. B. & Yang, S. Y. Research on single-crystal-to-single-crystal photoaddition and extension of Schmidt's rule in topological chemistry. *CrystEngComm* **25**, 3714–3717 (2023).
45. Thaksen, J. et al. Transformation between 2D and 3D covalent organic frameworks via reversible [2 + 2] cycloaddition. *J. Am. Chem. Soc.* **142**, 8862–8870 (2020).
46. Acharjya, A., Pachfule, P., Roeser, J., Schmitt, F. J. & Thomas, A. Vinylene-linked covalent organic frameworks by base-catalyzed aldol condensation. *Angew. Chem. Int. Ed.* **58**, 14865–14870 (2019).
47. Tu, M. et al. Reversible optical writing and data storage in an anthracene-loaded metal-organic framework. *Angew. Chem. Int. Ed.* **58**, 2423–2427 (2018).
48. d'Agostino, S., Spinelli, F., Boanini, E., Braga, D. & Grepioni, F. Single crystal to single crystal [2+2] photoreactions in chloride and sulphate salts of 4-amino-cinnamic acid via solid-solution formation: a structural and kinetic study. *Chem. Commun.* **52**, 1899–1902 (2016).
49. Yan, B., Shi, R., Zhang, B. & Kshirsagar, T. A kinetic study of product cleavage reactions from the solid phase by a biocompatible and removable cleaving reagent, HCl. *J. Comb. Chem.* **9**, 684–689 (2007).
50. Pandolfi, L. et al. The impact of solid solution composition on kinetics and mechanism of [2+2] photodimerizations of cinnamic acid derivatives. *CrystEngComm* **23**, 1352–1359 (2021).
51. Zhao, X. Q. et al. A simple approach to achieve organic radicals with unusual solid-state emission and persistent stability. *CCS Chem.* **4**, 1912–1920 (2022).
52. Li, T. et al. One-dimensional alkylate-bridged wüster's blue-based diradical dications. *Sci. China Chem.* **60**, 602–606 (2017).
53. Zhang, J. et al. How to manipulate through-space conjugation and clusteroluminescence of simple AIEgens with isolated phenyl rings. *J. Am. Chem. Soc.* **143**, 9565–9574 (2021).
54. Zhang, H. et al. Why do simple molecules with “isolated” phenyl rings emit visible light? *J. Am. Chem. Soc.* **139**, 16264–16272 (2017).
55. Frisch, M. J. et al. *Gaussian 09, Rev. D.01* (Gaussian, Inc., 2009).
56. Weigend, F. & Ahlrichs, R. Balanced basis sets of split valence, triple zeta valence and quadruple zeta valence quality for H to Rn: design and assessment of accuracy. *Phys. Chem. Chem. Phys.* **7**, 3297–3305 (2005).
57. Weigend, F. Accurate coulomb-fitting basis sets for H to Rn. *Phys. Chem. Chem. Phys.* **8**, 1057–1065 (2006).
58. Grimme, S., Ehrlich, S. & Goerigk, L. Effect of the damping function in dispersion corrected density functional theory. *J. Comput. Chem.* **32**, 1456–1465 (2011).
59. Andrae, D., Häußermann, U., Dolg, M., Stoll, H. & Preuß, H. Energy-adjusted ab Initio pseudopotentials for the second and third row transition elements. *Theor. Chim. Acta* **77**, 123–141 (1990).
60. Lu, T. & Chen, F. Multiwfn: a multifunctional wavefunction analyzer. *J. Comput. Chem.* **33**, 580–592 (2012).
61. Humphrey, W. F., Dalke, A. & Schulten, K. VMD: Visual molecular dynamics. *J. Mole. Graph.* **14**, 33–38 (1996).
62. Spackman, M. A. & Jayatilaka, D. Hirshfeld surface analysis. *CrystEngComm* **11**, 19–32 (2009).
63. Neese, F. Software update: the ORCA program system-version 5.0. *WIREs Comput. Mole. Sci.* **12**, e1606 (2022).

Acknowledgements

The authors thank the National Natural Science Foundation of China (No. 22271203 to J.P.L.), the State Key Laboratory of Organometallic Chemistry of Shanghai Institute of Organic Chemistry (No. KF2021005 to J.P.L.), the Collaborative Innovation Center of Suzhou Nano Science and Technology, the Priority Academic Program Development of Jiangsu Higher Education Institutions, the Project of Scientific and Technologic Infrastructure of Suzhou (No. SZS201905 to J.P.L.), Soochow University Starting Grant (NO. NH10902123 to Q.L.) and Postgraduate Research & Practice Innovation Program of Jiangsu Province (NO. KYCX22_3184 to M.F.W.).

Author contributions

M.F.W., Q.L. and J.P.L. conceived and designed the experiments. M.F.W. conceived and carried out experiments, determined structures, analyzed data, and corrected the draft of the paper. J.H.G. and Y.X.H. assisted in the fluorescence spectra data. Y.H.D. and Y.Y.C. performed DFT calculations. M.F.W., Q.L., P.B. and J.P.L. analyzed data and wrote the manuscript. All authors contributed to the discussion and revision of the paper.

Competing interests

The authors declare no competing interests.

Additional information

Supplementary information The online version contains supplementary material available at <https://doi.org/10.1038/s41467-023-42604-9>.

Correspondence and requests for materials should be addressed to Qi Liu or Jian-Ping Lang.

Peer review information *Nature Communications* thanks Panče Naumov, Kumar Varoon Agrawal and the other, anonymous, reviewer(s) for their contribution to the peer review of this work. A peer review file is available.

Reprints and permissions information is available at <http://www.nature.com/reprints>

Publisher's note Springer Nature remains neutral with regard to jurisdictional claims in published maps and institutional affiliations.

Open Access This article is licensed under a Creative Commons Attribution 4.0 International License, which permits use, sharing, adaptation, distribution and reproduction in any medium or format, as long as you give appropriate credit to the original author(s) and the source, provide a link to the Creative Commons licence, and indicate if changes were made. The images or other third party material in this article are included in the article's Creative Commons licence, unless indicated otherwise in a credit line to the material. If material is not included in the article's Creative Commons licence and your intended use is not permitted by statutory regulation or exceeds the permitted use, you will need to obtain permission directly from the copyright holder. To view a copy of this licence, visit <http://creativecommons.org/licenses/by/4.0/>.

© The Author(s) 2023